Sabrina Ferrari[a,b,*], Alessandro Maturilli[b], Cristian Carli [c],

Mario D'Amore[b], Jörn Helbert [b], Fabrizio Nestola [d], Harald Hiesinger [e]

# Thermal Infrared Emissivity of Felsic-rich to Mafic-rich Analogues of Hot Planetary Regoliths.

[a] Center of Studies and Activities for Space (CISAS) "G. Colombo", University of Padova, Via Venezia 15, 35131 Padova, Italy

[b] German Aerospace Center (DLR), Institute for Planetary Research, Rutherfordstraße 23, 12489 Berlin, Germany.

[c] National Institute for Astrophysics (INAF), Institute for Space Astrophysics and Planetology, Via Fosso del Cavaliere 100, 00133 Roma , Italy.

[d] Department of Geosciences, University of Padua, via Gradenigo 6, 35131 Padova, Italy.

[e] University of Münster, Institute for Planetology, Wilhelm-Klemm-Str. 10, 48149 Münster, Germany

*Corresponding author (e-mail: sab.ferrari@gmail.com)

## Abstract

Atmosphere-less inner Solar System bodies such as Mercury and several high-eccentricity Near Earth Objects use to undergo to a wide range of surface temperatures. The work shows how the thermal expansion induced by strong diurnal insolations affects the thermal infrared spectra of felsic-rich to mafic-rich regoliths. 1400-700 $cm^{-1}$ spectra of granular plagioclase-pyroxene mixtures were measured in laboratory at five temperatures between 295 K (ambient) and 725 K, simulating different daily surface temperatures of the Solar System. At the same time, the work describes for the first time how two minerals with different thermal expansion coefficients combined in the same granular sample reveal in a non-ambient thermal infrared spectrum. Spectra of plagioclase-rich analogues, on one hand, appear

dominated by felsic features regardless the surface daily temperature, and do not exhibit short-wavenumber absorptions of pyroxenes at all. When perceivable, on the other hand, the 920-$cm^{-1}$ clinopyroxene absorption, which use to be unaffected by thermal variations, proves instead to be a proxy for the solid-solution composition (i.e. Mg-Fe relative content). On the contrary, hints on the plagioclase solid solution occurring at ambient temperatures (i.e. Ca-Na relative content) disappear over 525 K. For all the mixtures, the position of the Christiansen Feature is linearly dependent on the plagioclase-pyroxene content as well as on the temperature, proving to be a reliable tool to obtain the relative mineralogical content when the surface temperature is known. As a whole, in order to decipher planetary hyperspectral data, the surface temperature acquisition seems to be mandatory, as well as the comparison with analogue spectra obtained under realistic temperature conditions.

Keywords: planetary - silicate – plagioclase – pyroxene - emissivity – temperature

## 1. Introduction

Compositional studies of planetary surfaces are mostly realized by means of the collection and interpretation of the released electromagnetic radiations. Ground-based, orbit and lander hyperspectral instruments covering a wide range of wavelength has allowed unveiling, locally or globally, the chemical and mineralogical surface properties of several rocky planetary bodies. Among these techniques, the thermal infrared (TIR, 100-5000 $cm^{-1}$) spectroscopy allows to recognize the mineralogical structures of the outer shell of crystalline assemblages. This capability mainly relies on the characteristic spectral features arising by cation–anion and lattice vibrations of crystalline structures in the middle portion of electromagnetic spectrum (Farmer, 1974). This technique works very effectively for silicates (Hamilton, 2010), for which

53 a few mineral groups - such as plagioclase feldspars - can be deficient in transition
54 elements and use to provide weak diagnostic features along shorter wavelengths (i.e.
55 visible and near-infrared wavelength).

56 By using TIR spectroscopy, compositional mapping is conducted at different
57 scales on several rocky bodies in the Solar System, primarily on the Earth surface
58 where remote sensing techniques can be easily combined with field data (Salisbury,
59 J.W., D'Aria, 1994). Earth-based observations in the TIR have been performed to
60 investigate surface components of both Main-belt and Near-Earth asteroids (e.g., Lim
61 et al., 2005; Vernazza et al., 2010) or inner planets (e.g., Sprague et al., 2009). On the
62 other hand, large-scale and global mapping are easier accomplished with orbital
63 surveys. Global mineral maps have been produced for example using Mars thermal
64 infrared data from the Mars Global Surveyor Thermal Emission Spectrometer (TES,
65 Christensen et al., 2001) and the Mars Odyssey Thermal Emission Imaging System
66 (THEMIS, Christensen et al., 2005), and using lunar data from the Lunar
67 Reconnaissance Orbiter (LRO) Diviner (Greenhagen et al., 2010). A new frontier of
68 the Solar System exploration is the return of solid samples from asteroids, which is
69 accomplished through a preliminary global survey to find suitable sampling sites and
70 minimize risks during the surface campaign. For instance, Near Earth Asteroid
71 (101955) Bennu is the target of the Origins, Spectral Interpretation, Resource
72 Identification, and Security–Regolith Explorer (OSIRIS-REx) asteroid sample return
73 mission (Lauretta et al., 2017). During the first two-year orbit period (2018-2019), the
74 global survey of Bennu is correlated by the OSIRIS-REx Thermal Emission
75 Spectrometer (OTES, Christensen et al., 2018) that provides the surface mineralogy
76 through 100-1750 $cm^{-1}$ emissivity spectra.

In order to succeed in the interpretation, the correlation of remote sensing data to a solid laboratory background is crucial. A great effort has been done to directly obtain the emissivity of a sample radiative surface, and specific laboratory setups and databases have been built up to sustain the remote Solar System exploration. In support of NASA Mars missions, an extensive library containing thermal emission spectra of coarse-grain rocks and minerals undergone 350 K has been supplied by the Arizona State University (ASU, Christensen et al., 2000). Matching orbital spectra with the ASU laboratory spectra (Hamilton and Christensen, 2000) allowed mapping silicate assemblages on the Mars surface (Bandfield et al., 2000; Ramsey and Christensen, 1998). Similar analysis techniques were applied on lunar soils, using LRO Diviner radiometer channels (Paige et al., 2010) to investigate a diagnostic emissivity maximum called Christiansen Feature (CF, Conel, 1969). CF positions detected by Diviner were compared to the CF positions of well-characterized lunar samples and analogues, obtaining a global map of the silicate dominant phases (Greenhagen et al., 2010). Lunar environment, as long as other airless environments, promotes strong thermal gradients within the shallow radiative depth, affecting CF positions (Glotch et al., 2010). Being feldspar CFs proper proxies of primary anorthositic crust, plagioclase analogues were widely studied in laboratory along the TIR range under different environment conditions (Donaldson Hanna et al., 2012), then used for Moon Mineralogy Mapper data interpretation (Donaldson Hanna et al., 2014).

In support of the future employ of BepiColombo Mercury Radiometer and Thermal Infrared Spectrometer (MERTIS, Hiesinger and Helbert, 2010) on the ESA-JAXA BepiColombo mission, the Planetary Spectroscopy Laboratory (PSL, www.dlr.de/pf) of the German Aerospace Center (DLR) has developed a simulator

chamber that allows to increase the temperature of the sample radiative depth up to ~775 K – comparable to the maximum temperature reachable at the equator of Mercury - in a vacuum environment. A Fourier spectrometer equipped with a nitrogen cooled detector coupled to the chamber allows measuring emissivity of a variety of particle sizes of possible surface Mercury analogs. Those measurements, along more traditional low-temperature emissivity measurements in purged environment, constitute the Berlin Emissivity Database (Maturilli et al., 2008). Recent works that combine accurate lattice data to PSL emissivity spectra of olivine and clinopyroxenes (Ferrari et al., 2014; Helbert et al., 2013) demonstrate that the thermal expansion promoted by intense daily insulation of a planetary surface (e.g., of Mercury) induces variations on spectral features. Though those spectral variations are strictly correlated to the temperature variation and totally reversible, they provide a temporary mismatch between space data and traditional databases, affecting the correct interpretation of the surface composition as much as irreversible transformations (e.g., spectral flattening due to shock impacts) affect possible structural inferences (e.g., particle size). Basic variations characterized in PSL spectra during the thermal expansion imply the shift of most features, simulating an increasingly size of the main cations, and the quasi-steady state of others, the latter of which can be considered baselines for any interpretation. A more difficult interpretation of the spectra, of course, arises from the simultaneous presence of different minerals during thermal expansion, since each mineral bears a different thermal expansion coefficient.

In this work we examine the TIR spectral variations of bimodal mixtures of plagioclase and pyroxene, which most likely could be present on a planetary silicate surface, in addition to the temperature-dependent spectral variations of the single constituents, regardless their formational mechanism. The study is specifically

127 focused on absorption features with wavenumbers between 1400 and 700 $cm^{-1}$ (7-14
128 μm), where the most prominent silicate bands are observed. In this range, absorptions
129 mainly occur by the stretching vibrations of the cation-oxygen (Si/Al-O) tetrahedra.
130 With increasing temperature, though tetrahedra represent the stiffer configuration of
131 silicate, the entire structure uses to adjust in order to maintain the linkage between
132 different polyhedra layers. This adjustment results in a change of bond lengths of
133 Si/Al and surrounding oxygens, a change reflected in the stretching potential of each
134 of those bonds. In order to investigate how those variations promoted by thermal
135 expansion affect the 1400-700 $cm^{-1}$ spectral range, we measured at different steps of
136 temperature - up to 725 K – the emissivity of co-genetic silicates with different weight
137 ratio, reduced to suitable particle sizes for the regolith of a rocky planetary body.

138 ## 2. Methods

139 ### 2.1 Selection, preparation and characterization of the samples

140 To better constrain the effect of different variables acting on surface materials
141 it is useful to consider *ad hoc* samples to separate as much as possible the single
142 components. Bimodal mixtures with variable abundance of co-genetic endmembers at
143 constrained particle sizes is suitable for this purpose.

144 Plagioclase and pyroxene are among the most diffuse silicates of the Solar
145 System. In particular, terrestrial planet that underwent to a primordial differentiation
146 accumulated floating plagioclases dragging low amounts of mafic minerals on the
147 outermost shell (e.g., Halliday, 2001; Tonks and Melosh, 1993; Wetherill, 1980). In
148 addition, plagioclase and pyroxene are the most abundant phases of lava flow rocks,
149 which are currently considered the main constituents of the Mercury's crustal surface
150 (Namur and Charlier, 2017 and reference therein), and S-type asteroids (e.g.,
151 Nakamura et al., 2011). Therefore anorthosites-kindred materials represent a suitable

152 analogue of an elementary bimodal combination of differently polymerized silicates
153 bearing different thermal expansion coefficients.

154 The set of considered mineral endmembers consists of single phases occurred in
155 a natural anorthosite sample belonging to the gabbro-anorthosite Nordingrå complex
156 (Sweden, Lindh et al., 2001). This massif displays a high percentage of outcropping
157 leucogabbro and true anorthosite with respect to other rapakivi-type massifs - possibly
158 depending on a multiple intrusion mechanism - favouring the collection of feldspar-
159 rich samples. Typical Nordingrå-complex anorthosite is coarse-grained and has a
160 plagioclase content higher than 90 wt%. Plagioclase crystals can reach 1–4 cm in
161 length: their compositional range is $An_{48–67}$, with labradorizing cores. Clinopyroxene
162 ($Di_{60}$) and olivine are the main primary mafic minerals, frequently substituted by
163 uralitic hornblende. Brown biotite and opaque minerals as ilmenite and magnetite
164 occur as inclusions.

165 A unique bulk sample of anorthosite was used to provide co-genetic single-
166 mineral phases suitable for weighted linear mixtures. The sample bulk composition
167 was analysed by X-ray powder diffraction at the Department of Geosciences of the
168 University of Padua. Data were recorded on a PANalytical θ-θ diffractometer (Cu
169 radiation) equipped with a long fine-focus Cu X-ray tube operating at 40 kV and 40
170 mA and a real-time multiple strip (RTMS) detector (X'Celerator). The scan was
171 performed over the range 3–80° 2θ with a step size of 0.017° 2θ and a counting time
172 of 150 s/step. The program High Score Plus (PANalytical) was used for phase
173 identification and quantitative phase analysis with Rietveld refinement (Rietveld,
174 1967). A pseudo-Voigt function was employed for the profile shapes. Refined
175 parameters were scale factors, zero-shift, background, lattice constants, and profile
176 parameters (Gaussian and Lorentzian coefficients). Results of the analysis are

177 reported in Table 1SM. Plagioclase solid solution ranges between andesine and
178 labradorite ($An_{70-30}$), and represents the 83 wt% of the analysed material.
179 Clinopyroxene (ferroan diopside 6 wt%) is partially substituted by uralitic amphibole
180 (actinolite) and chlorite. Quartz and ilmenite are detectable, whereas shallow peaks of
181 low-calcium pyroxene and biotite are observable but not quantifiable.

182 The bulk sample was divided into two equal volumes that were mechanically
183 ground in a jaw crusher toward 1 mm, obtaining two partitions of anorthosite
184 *talquale*. Those partitions represent samples where the relative abundance of
185 plagioclases and clinopyroxenes are 93% and 7%, respectively. In order to separate
186 pyroxenes from the sialic minerals, a mechanical separation of additionally-reduced
187 grain sizes (e.g., by Frantz Magnetic Separator) was considered ineffective because of
188 the widespread presence of amphiboles. Then 0.5 to 1-mm plagioclase and pyroxene
189 crystals were separated by hand-picking from one of the two anorthosite-*talquale*
190 partitions. Though sericitization was diffuse, preserved crystals of the required phases
191 were still available. Plagioclase crystals displayed diffuse labradorescence, and the
192 occasional quartz were accompanied by chalcopyrite-pyrite coatings. Well-shaped
193 augites were distinguishable by elongated amphiboles and tabular brown biotite.
194 Mafic crystals were often accompanied by euhedral small apatites, which have been
195 carefully discarded.

196 Crystals of the two picked phases were analysed by the wavelength-dispersive
197 system (WDS) method. The analyses were carried out using a CAMECA CAMEBAX
198 SX50 electron microprobe, with a fine-focused beam (~1 μm diameter), an
199 acceleration voltage of 20 kV and a beam current of 20 nA, with 10 s counting times
200 for both peak and total background. Ten analytical spots per sample were acquired. X-
201 ray counts were converted to oxide wt% using the PAP correction program supplied

202 by CAMECA (Pouchou and Pichoir, 1991). Results of the analyses are reported in
203 Table 2SM. Plagioclase solid solution ranges between $An_{45}$ and $An_{65}$, possibly
204 confirming crystal cores enriched in Ca, whereas clinopyroxenes display lower
205 content of Ca, and much variable Mg# (i.e. 0.33-0.52) with respect to the value
206 reported by Lindth et al. (2001).

207 All partitions (i.e. anorthosite *talquale*, plagioclase and clinopyroxene phases)
208 are further reduced in a dry planetary ball mill using sintered aluminium oxide balls,
209 and sieved to <63 and 63-125 µm size fractions. In the attempt to reduce size-
210 distribution differences induced by hardness, final samples were obtained mixing a
211 part of <63-µm fraction and a part of 63-125-µm fraction, in a weight ratio of 1:1. The
212 particle-size fraction of <125 µm, provided for the spectroscopic measurements,
213 cannot be totally immune to thermal gradient and multiple scattering effects in the
214 TIR range (Maturilli et al., 2006 and reference therein), nevertheless it approaches the
215 finest Moon and Mercury's regolith size (Emery et al., 1998; Mckay et al., 1980). In
216 particular, the <63-µm fraction is numerically dominated by finest particles, possibly
217 reaching the 70 wt% constituted by particles <5 µm in diameter. Such finest
218 particulate, smaller than the studied wavelength range, uses to coat larger particles
219 dominating the spectral behaviour of the overall sample (Salisbury and Wald, 1992).

220 Two suitable analogues of bi-components were obtained mixing 90 wt% of
221 plagioclases with 10 wt% of clinopyroxene, partly comparable with the anorthosite
222 *talquale* (i.e. 93% and 7%, respectively), and mixing 50 wt% of plagioclase with 50
223 wt% of clinopyroxenes. This intermediate assemblages can be associated to a first
224 case study where plagioclase and mafic materials are mixed in equal abundances
225 similar to some of the normative Mercury-like terrain (e.g., E. Vander Kaaden et al.,
226 2017). The achieved samples set, which includes the Nordingrå-complex anorthosite

(*anorth*), the plagioclase endmember (*pl100*), the pyroxenes endmember (*pl000*), the 90-wt% plagioclase mixture (*pl090*) and the 50-wt% plagioclase mixture (*pl050*), is summarized in Table 1. Samples available for measurements were placed into

(i) teflon cups, operating for vacuum reflectance measurements, with a 10 mm internal diameter and 2 mm thick bottom, filling the cups for the whole available volume, and

(ii) stainless steel cups operating for vacuum high-temperature measurements, with a 50 mm internal diameter, 5 mm thick bottom and 20 mm in height, filling the cups for the first 3 mm.

Filled cups were placed in a dryer chamber.

### 2.2 Experimental setup

The spectral measurements were performed at the PSL. The instrument used was a Bruker Vertex 80V FTIR spectrometer operated under vacuum, with liquid nitrogen cooled HgCdTe detector and KBr beamsplitter. Emissivity and reflectance spectra were acquired between 750 and 1400 $cm^{-1}$, at a spectral resolution of 4 $cm^{-1}$.

The external evacuated planetary simulation chamber was used to measure emissivity. The setup provides that the steel cup containing the sample is heated via an induction system and the radiance is collected by an Au-coated parabolic 90° off-axis mirror and reflected to the spectrometer. Samples were heated once and emissivity was measured under a medium vacuum of 0.7 mbar at 425 K, 525 K, 625 K and 725 K with increasing temperatures, then during the cooling maintaining the temperature at 525 K. Measurements of the calibration body were taken at the same temperatures as the sample. Within the chamber, an iron buffer was provided in order to avoid any possible iron oxidation during the annealing. The intent of this setup was

to reach the maximum temperature variation achievable by the PSL setup within the range suggested for terrestrial planet surfaces, preventing any possible variation of the sample during the heating. The sample radiance $I_{(T)}$ and the calibration body radiance $CB_{(T)}$ were collected at each scheduled step of temperature *T*. For each sample, 5 scans were averaged to produce a single spectrum. The absolute emissivity of the sample $\varepsilon_{a(T)}$ is derived using the $\varepsilon_{a(T)} = I_{(T)} / CB_{(T)} \cdot E_{CB}$, where $E_{CB}$ is the calibration body emissivity curve. More details regarding the setup and the calibration technique are discussed in Ferrari et al. (2014).

A Bruker A513 accessory was used for bi-conical (illumination=emission=13°) reflectance measurements (Maturilli et al., 2014) at room temperature. The bi-directional reflectance of each sample (R) was collected in medium vacuum at 295 K within the same range of wavelength. A derived emissivity $\varepsilon_d$ is obtained following the Kirchhoff's law [$\varepsilon_d = 1- R$] for a comparison with the measured $\varepsilon_a$ at low temperature.

## 3. Results

In this work the influence of the simulated environment on measured spectra is described in terms of spectral contrast referring to the imposed vacuum, and of absorption band wavenumber position referring to induced thermal expansion. In the 700-1400 $cm^{-1}$ wavenumber range, the spectral contrast between the CF and the first group of absorption features, as well as the wavenumber position of the CF relative to the absorption bands, are strongly affected by the decreasing pressure and the increasing thermal gradients (Donaldson Hanna et al., 2012 and reference therein; Logan et al., 1973). Concerning the spectra of end-member phases, emissivity absorption minima previously described in the literature as diagnostic are identified as (i) reststrahlen bands (here referred as RB) due to the Si-tetrahedral fundamental

276 vibrations (Lyon, 1962), and (ii) transparency features (TF) caused by volume
277 scattering characteristic of fine particle sizes (Maturilli et al., 2006; Salisbury and
278 Walter, 1989). Reststrahlen bands have long been identified as diagnostic of
279 composition (e.g., Lyon, 1962).

280 Measured spectra are shown in Figures 1 and 2, including reflectance-derived
281 emissivity (orange line). Figure 1 shows the spectra of the Nordingra-complex
282 anorthosite (*anorth*), which represents a relative abundance of 93% of plagioclases
283 and 7% of clinopyroxenes (Table 1). In Figure 2, spectra of plagioclase (*pl100*) and
284 pyroxenes (*pl000*) end-members and samples obtained by mixing (*pl090* and *pl05*0,
285 Table 1) are displayed, from left to right, with increasing pyroxene content and
286 decreasing degree of polymerisation of the silicate structures, i.e. decreasing
287 cumulative number of oxygens shared by tetrahedra. The polymerisation uses to
288 strengthen the structure, increasing the CFs values and the spectral contrasts (e.g.,
289 Logan et al., 1973), and driving the main absorption features toward higher
290 wavenumbers (or higher frequencies of vibration, requiring more energy to vibrate;
291 Farmer, 1974; Salisbury and Walter, 1989). All spectra of measured emissivity
292 display an ubiquitous rise at 1370 $cm^{-1}$ due to a shallow absorption of the calibration
293 body. Documented diagnostic features of reflectance-derived emissivity spectra
294 collected at 295 K are listed in Table 2, in terms of CF locations and absorption-band
295 minima positions, and in Table 3 as emissivity values. Corresponding diagnostic
296 features of measured emissivity spectra are listed in Table 4, in terms of CF locations
297 and absorption-band minima positions, and in Table 5 as emissivity values.

298 The end-member phases are considered reference samples for the spectral
299 interpretation. From higher to lower wavenumbers, the spectral features attribution of
300 the plagioclase end-member (*pl100*, Figure 2) includes the CF, two close reststrahlen

bands (RBs) between 1100 and 1200 $cm^{-1}$ followed by a third one located at ~1000 $cm^{-1}$, and a transparency feature (TF). The shallow RB located at 920 $cm^{-1}$, which is equally characteristic of plagioclase solid solutions, appears overlapped with the deep TF of plagioclase-bearing samples. Concerning low-temperature spectra (i.e. spectra collected at 295 and 425 K), the split of the high-wavenumber broad reststrahlen band in two minima and the occurrence of the TF at ~870 $cm^{-1}$ are characteristics of Na-rich plagioclase solid solutions (Donaldson Hanna et al., 2012; Hamilton and Christensen, 2000), and consistent with the andesine content of *pl100* sample (Table 1SM). Similarly, the spectral features attribution of the clinopyroxenes end-member (*pl000*, Figure 2) includes the CF, three RBs at ~860, ~950 and ~1100 $cm^{-1}$, and a TF. Concerning low-temperature spectra (i.e. spectra collected at 295 and 425 K), the asymmetry of the first RB and the location of the third RB at ~870 $cm^{-1}$ are characteristic of Fe-rich augites (Hamilton, 2000), and consistent with $Mg_{0.33}$- and $Mg_{0.52}$-clinopyroxenes of *pl000* sample (Table 2SM). Consistently with the different degree of polymerisation, plagioclase RBs occur at higher wavenumbers with respect to the pyroxene ones because of their higher number of oxygens shared by two tetrahedral (Smith and Brown, 1988). In general, low-temperature TFs are deeper than RBs.

Low-temperature spectra of synthetic anorthosite (*pl090*) and anorthosite *talquale* (*anorth*) appear strongly influenced by the plagioclase content, displaying as well the CF, the two close RBs followed by a third one and the TF (Figure 1 and 2). Comparing the two samples, variations of the absorption positions can be attributed to a different wt.% of the main phases and to the secondary phases detectable in the parental body. *Anorth* sample, indeed, implies a 6 wt.% content of quartz, which spectrally shifts the CF toward lower wavenumbers and increases the separation

between the first two RBs with respect to *pl090* sample (Wald and Salisbury, 1995). On the other hand, low-temperature spectra of the synthetic gabbro (*pl050*), which is constituted by the same weight of plagioclase and clinopyroxene, show a series of features of more complex interpretation (Figure 2). Christiansen features of *pl050* spectra appear sharper than CFs of all other samples. The spike shape depends on the presence of equal amount of two minerals that significantly differ along this short range. The sum of the optical contributions does not perform with a broadening of the CF, which on the contrary manifests where the refractive index of both minerals approaches the medium refractive index (overlapping zone). *Pl050* spectra show reststrahlen bands of both end-members (Figure 2 and Table 2 and 4), with the last one (the fourth RB) coinciding with the TF characteristic of plagioclases and followed by the TF characteristic of pyroxenes. A general shift of all absorption bands toward lower wavenumbers (i.e. lower vibrational frequencies) with decreasing plagioclase content accommodates the contribution of less polymerized materials as pyroxenes.

The overall low spectral contrast that occurs between CFs and Si(/Al)-tetrahedral absorption bands (RBs), which is quantifiable around 2-5 percent variation, and the persistence of transparency features in low-pressure environments (Figure 1 and 2) are due to the dominant fine fraction of all samples that induces a volume scattering regime (Maturilli et al., 2006; Salisbury and Wald, 1992). End-member spectra tend to display greater spectral contrast than mixtures in which they occur (e.g., Hamilton and Christensen, 2000). Absolute emissivity collected at low temperature (i.e. 425 K) and derived emissivity (reflectance collected at 295 K) show comparable features, though for the absolute-emissivity measurements the spectral contrast appears attenuated and the CFs of plagioclase-rich samples tend to broad and shift toward higher wavenumbers with respect to the derived-emissivity CFs (Figures

351 1,2). A decreased spectral contrast can be attributed to substantial differences in the
352 measure techniques, e.g. to a less stable vacuum state of the emissivity measurements.
353 A lower vacuum, indeed, uses to promote a general decline of the spectral contrast
354 (e.g., Donaldson Hanna et al., 2012). The shift shown by the CFs of plagioclase-rich
355 samples is most likely due to the stronger thermal gradient promoted by the increased
356 temperatures along the radiative depth (Salisbury and Walter, 1989). Conversely, no
357 shift (<$cm^{-1}$) occurs for CF peak of *pl000* sample (Figure 2), which toward higher
358 wavenumbers displays a broad shoulder that possibly depends on a preferential
359 orientation of the particles with respect of the radiative surface, an expected behaviour
360 for chain silicates such as pyroxenes. Being *pl050* sample composed by 50-wt% of
361 both end-members, the CF position of its spectra is strongly influenced by the
362 effective composition of the radiative surface, therefore it could be difficult to
363 compare spectra originated from different sample cups.

364 Concerning the emissivity spectra shape, with increasing temperatures two main
365 variations are observed (Figures 1, 2): (i) the spectral contrast between CFs and the
366 RBs increases; (ii) the emissivity maximum located around 800 $cm^{-1}$ notably
367 decreases, resulting in an increase of negative slope between the two maxima.
368 Donaldson Hanna et al. (2012) highlighted that an increase of the spectral contrast is
369 correlated to an increase of the vacuum level. Therefore, the overall increase of
370 spectral contrast with increasing temperature of Figs. 1 and 2 measurements could be
371 partially influenced by an increased vacuum within the emissivity chamber.

372 As well as done for the end-members, the main spectral features of emissivity
373 spectra (i.e. CFs, RBs and TFs) can be discussed in function of temperature and
374 plagioclase's relative abundance.

375 CFs tend to shift toward higher wavenumbers with increasing temperatures
376 (Figures 1,2,3). In particular, plagioclase-rich CFs shift from 1280-1291 $cm^{-1}$ to 1300-
377 1314 $cm^{-1}$, with an average shift of 20 $cm^{-1}$ from 425 K to 725 K. CF's pyroxene end-
378 member located at 1160 $cm^{-1}$ displays no significant changes up to 625 K, then shifts
379 of about 30 $cm^{-1}$ to the highest temperature (Figure 3). On the other hand, synthetic-
380 gabbro spectra show a systematic shift of the CF, gaining 30 $cm^{-1}$ (i.e. from 1240 $cm^{-1}$
381 to 1273 $cm^{-1}$). The greater CF shifts of pyroxene-rich spectra are consistent with
382 results of Logan et al. (1973). The systematic shift of plagioclase-bearing CFs with
383 increasing temperature is even better highlighted in Figure 3, where each
384 "temperature" set of measurements (differentiated by colours) shifts consistently
385 toward higher wavenumbers. Similarly to the absorption features, the CF position
386 uses to shift toward lower wavenumbers with decreasing polymerization, i.e. from
387 plagioclase to pyroxene (Farmer, 1974): CFs shown in Figure 3 consistently shift.
388 Due to the fact that up to 725 K the position of all measured CFs does not overlap,
389 this features are considered diagnostic of the plagioclase-pyroxene ratio.

390 In order to compare the behaviour of the main absorption bands consequently to
391 the temperature and compositional variations, the reststrahlen bands of all emissivity
392 spectra have been grouped depending on their wavenumber occurrence (Figures 1,2).
393 Within the 1400-700 $cm^{-1}$ range, four wavenumber windows have been reasonably
394 identified as representative of RBs occurrence for our samples' set (grey windows,
395 Figures 1,2). The first two windows refer to the two close high-wavenumber RBs that
396 characterize the plagioclase end-member spectra: the 1160-1190 $cm^{-1}$ window
397 (labelled *a* in Figures 1,2) includes all the first RBs developed along the entire
398 temperature range by samples containing plagioclase, the 1080-1150 $cm^{-1}$ window
399 (labelled *b* in Figures 1,2) comprehends the second RBs of samples containing

400 plagioclase as well as the first RBs of the pyroxene end-member, which occurs
401 between 1085 and 1105 $cm^{-1}$ (Figures 1,2,4). The third window, located in the 940-
402 1000 $cm^{-1}$ range (labelled *c* in Figures 1,2), refers to the third RBs of samples
403 containing plagioclase and the second RBs of the pyroxene end-member, which
404 overlap in the synthetic-gabbro sample spectra (i.e. *pl050*). The fourth window,
405 located in the 850-880 $cm^{-1}$ range (labelled *d* in Figure 2), refers to the third RBs of
406 the pyroxene end-member, which likewise occurs in *pl050*.

407 RBs occurring at ~920 $cm^{-1}$ (Figures 1,2), which are characteristic of
408 plagioclase solid solutions, appear strongly affected by the TF of plagioclase-bearing
409 samples and therefore less reliable. Their positions do not show significant shifts with
410 increasing temperature or plagioclase content (Table 4). Nevertheless, their spectral
411 slope tends to increase with increasing temperature (Table 5), allowing to prevail on
412 the TF over 725 K.

413 Figure 4 allows a comparison of the main emissivity RB minima's shifts as
414 function of the temperature variation and of the plagioclase content. High-
415 wavenumber RBs located within the *a* window - and characteristic of samples
416 containing plagioclase - systematically shift toward lower wavenumbers (i.e. negative
417 shift, Figure 4a) with increasing temperatures, disappearing over 525 K in the
418 plagioclase end-member (*pl100*) spectra and over 625 K in the synthetic anorthosite
419 (*pl090*) spectra. Shifts of those RBs are linear and can be quantified in a decrease of
420 8-10 $cm^{-1}$ per 100 K/degrees of increasing temperature (i.e. ~$10^{-1}$ $cm^{-1}$ $K^{-1}$). On the
421 other hand, at the same temperature, plagioclase-rich absorptions occurring within this
422 first window shift toward higher wavenumbers with increasing plagioclase content
423 (i.e. with a positive shift, Figure 4d): in this specific comparison the anorthosite
424 *talquale* (*anorth*) features are interpreted to be dependent on the 83 wt.% of

425 plagioclase that constitutes the sample. Whereas the synthetic-gabbro (*pl050*) group
426 displays a negative shift with respect to the anorthosite *talquale* absorptions for most
427 of the temperature steps (Figure 4d), being influenced by the high content of pyroxene
428 that uses to show the first absorption at lower wavenumbers.

429 Concerning the *b* window, with increasing temperature RBs display negative
430 shifts as well (Figure 4b), but to a lesser extent with respect to the higher-
431 wavenumber RBs: shifts tend to increase with increasing content of pyroxene from 2-
432 3 $cm^{-1}$ per 100 K for *pl100* and *anorth* minima (i.e. 0 to 6 wt.% of pyroxene,
433 respectively) to 5-6 $cm^{-1}$ every 100 K for *pl050* and the pyroxene end-member (*pl000*)
434 minima. Within the *b* window, shifts are again strongly controlled by the pyroxene
435 content: an increase of pyroxene of 10 wt.% in plagioclase-rich samples corresponds
436 to a maximum shift of 8 $cm^{-1}$; an additional increase of 40 wt.% (*pl050*) corresponds
437 to an additional shift of about 35 $cm^{-1}$ (Figure 4e), whereas an additional increase of
438 50 wt.%, which correspond to the *pl000* sample, corresponds to a maximum increase
439 of 10 $cm^{-1}$. The gabbroic-like features, indeed, are conditioned by the lower-
440 wavenumbers attitude of the pyroxene end-member. Even in this case, it seems to be
441 clear the influence of the pyroxene on the absorption positions.

442 The *c* window includes the third RBs of plagioclase-bearing spectra and the
443 second RBs of the pyroxene end-member (Figures 1,2). With the first 100-K increase,
444 at 525 K the plagioclase-bearing features appear all shifted of different amount to
445 gather in a narrow interval between 985 and 989 $cm^{-1}$, whereas further increases of
446 temperature does not provide substantial changes on their positions (Figure 4c). On
447 the contrary, the third RB of *pl000* linearly shifts toward lower wavenumbers with a
448 decrease of ~4 $cm^{-1}$ per 100 K. With increasing temperature, the divergence of RB's
449 positions depending on the sample composition suggests that RBs occurring within

450 this window are strongly affected by the plagioclase content, which works as a
451 stiffener. On the other hand, low-temperature absorptions enclosed in the *c* window
452 tend to shift toward lower wavenumbers with increasing pyroxene content (Figure 4f),
453 roughly coupling the shift amount between *pl050* and *pl000* and confirming the
454 dominance of plagioclase within this range.

455 Concerning the third RB of the pyroxene end-member (*d* window, Figure 2),
456 which occurs as a fourth absorption in the *pl050* spectra, it seems to undergo as well a
457 negative shift of 9 $cm^{-1}$ with the first 100 K of temperature increase, and then notably
458 decreases the shifts to 3 $cm^{-1}$ per 100 K from 525 K to 725 K (Table 4).

459 Figure 5 allows a comparison of the main RB spectral contrasts (i.e. the
460 differences between the CF emissivity and the absorption-minima emissivity) as a
461 function of the temperature variation and of the plagioclase content. Spectral contrasts
462 between CFs and RBs increase both with increasing temperature, smoothing
463 differences due to the wavenumber position, and with increasing plagioclase content.
464 The increase reduces the evidence of the TFs and it appears linear and proportional to
465 the plagioclase content, being spectral contrasts of plagioclase-rich RBs twice the
466 pyroxene-rich values at low temperatures, and three times at high temperatures. Even
467 in this case, anorthosite-*talquale* RBs act as though the sample is composed by 83
468 wt.% of plagioclase, confirming the contribution of other components on the spectral
469 contrast. The minimum increase of spectral contrast occurs in pyroxene end-member
470 (*pl000*) spectra. The correlation between spectral contrast and plagioclase-pyroxene
471 ratio suggests that spectral contrast is not solely affected by vacuum efficiency, which
472 increases with increasing temperatures, but can be related to the mineralogy as well.
473 The mineralogical composition, indeed, can affect the thermal conductivity and the
474 average size of the sieved particulate. Concerning this work, a generally lower

475 spectral contrast of pyroxene's RBs is consistent with an enrichment in finer
476 particulates during the grinding (e.g., Logan et al., 1973), which is corroborated by
477 the presence of deeper TFs (Figure 2).

478 4. Discussion

479 In this work, in most cases, the position of the CF tends to shift toward higher
480 wavenumbers with increasing temperatures and toward lower wavenumbers with
481 decreasing polymerization (i.e. from plagioclase to pyroxene) (i) linearly and (ii)
482 without superimpositions, becoming a useful proxy even for mixtures, not only for
483 plagioclases.

484 With increasing temperatures, in the 900-1200 $cm^{-1}$ range, all RBs of the
485 considered samples show a shift of their position and a deepening with respect to the
486 CF emissivity values. Highest shifts are negative and occur at higher wavenumbers of
487 plagioclase-bearing spectra, but their extent does not depend on the plagioclase wt.%.
488 Those shifts, associated with an increased spectral contrast, are the most prominent
489 variations that, for example, an instrument like MERTIS can encounter for regoliths
490 dominated by plagioclase-clinopyroxene assemblages on the hot surface of Mercury.
491 Notably, at very high temperatures plagioclase-rich spectra lack of the high-
492 wavenumber RBs, similarly to those of the pyroxene end-member, therefore any
493 compositional interpretation must refer to the following RB positions. More moderate
494 negative shifts of the RB positions occur at lower wavenumbers, within the *b* window
495 (Figure 2), with extents that seem to be proportional to the pyroxene content. A
496 relationship between the RB's shift amount and the thermal expansion coefficient ($\alpha_V$)
497 of the single-phase mineral has been observed by Helbert et al. (2013) and Ferrari et
498 al. (2014) in silicate spectra. Within similar temperature ranges, a $An_{46}$-$Ab_{34}$
499 plagioclase - which is comparable to the *pl100* composition - has a $\alpha_V$ of $2.2\times10^{-5}$ $K^{-1}$

(Tribaudino et al., 2010), whereas a Fe-rich clinopyroxene - Mg# 0.17, which is closer to the *pl000* composition - has a $\alpha_V$ of $2.7\times10^{-5}$ $K^{-1}$ (Ferrari et al., 2014). In this work, the RB of *pl100* that occurs within the *b* window displays an average shift of about 2 $cm^{-1}$ per 100 K, whereas that one of *pl000* display an average shift of about 6 $cm^{-1}$, consistently with the idea that greater coefficients use to promote greater shifts. In any case, the position of the *b*-window RB, when complemented by the surface temperature, is useful to distinguish anorthosite-like mixtures (i.e. felsic-rich regolith) from the gabbroic-like or basaltic-like ones (i.e. more mafic compositions). This is also the case of MERTIS that, having a spectral resolution ranging from 9 to 20 $cm^{-1}$ in this spectral range, is sensitive both to great plagioclase-pyroxene ratio variations and to major temperature changes of the Mercury surface. On the other hand, RBs occurring at moderate to high temperatures at even lower wavenumbers (*c* window of Figure 2) are diagnostic of the plagioclase presence but cannot provide further information on the plagioclase-pyroxene ratio. The adjacent RBs, occurring at ~920 $cm^{-1}$, would be instead indicative of plagioclase-rich mixtures but are strongly affected by the closer TF. A distinction between anorthositic- and gabbroic-like regolith could be achieved through the spectral contrast at very high temperatures, but it would require a suitable knowledge of the involved surface parameters (grain size distribution, pressure, thermal gradient etc.) and possibly more analogue measurements. Lowest shifts are negative and occur at lower wavenumbers of pyroxene-rich spectra (i.e. within the *d* window). More precisely, the lowest shifts occur in the third RB of *pl000*, consistently with Ferrari et al. (2014). Concerning both the position and the spectral contrast, during MERTIS detection this feature would appear unaffected by the increase of temperature, therefore it is eligible to indicate pyroxene-rich regolith.

## 5. Conclusions

1400-700 $cm^{-1}$ emissivity spectra of bimodal mixtures of plagioclase and pyroxene measured between 425 K and 725 K have been examined in order to evaluate changes due to temperature and plagioclase-pyroxene ratio variations. In particular, the distinction of a plagioclase-rich regolith from more mafic compositions (e.g., gabbroic as well as basaltic) has been assessed, determining which features can be diagnostic during the remote sensing investigation of hot planetary surfaces. Results suggest that, regardless the surface daily temperature, spectra of anorthositic-like regolith can be distinguished from those of gabbroic-like regolith by the lack of absorptions at 850-880 $cm^{-1}$, which are characteristic of pyroxene-rich mixtures. In addition, a more robust distinction can be achieved cross-checking the wavenumber of the Christiansen features and the wavenumber of reststrahlen absorptions located between 1080 and 1150 $cm^{-1}$ with the temperature of the radiative surface. Noteworthy, spectra of plagioclase-rich regolith measured at high surface temperatures can lack of the first reststrahlen band, suggesting the contribution of a Ca-rich plagioclase instead of a more correct intermediate plagioclase solid solution. At high temperatures, on the other hand, the increase of spectral contrast of the reststrahlen absorptions to the detriment of the transparency feature makes items more readable, and the spectral contrast itself could be used to distinguish deeper plagioclase-rich absorptions. To be remarked that MERTIS laboratory performances (D'Amore et al., 2018) show signal-to-noise ratio greater than 200 in the 1000-1200 $cm^{-1}$ range, meaning that the noise level is lower than 0.5%. Such a performance would fully enabling MERTIS to detect on the hot surface of Mercury most of the variations shown in this work. On the other hand, the interpretation of the hyperspectral data returned by MERTIS as well as by any other TIR spectrometer will

benefit from laboratory spectra obtained under realistic temperature conditions, especially in cases where instruments measure the surface temperature independently with an integrated radiometer. Ongoing work focuses on both extending such measurements to more complex planetary-body analogues as well as a theoretical understanding of the thermal effects based on ab-initio calculations.

## Acknowledgments

We thank the Deutscher Akademischer Austausch Dienst (DAAD) and the Italian Space Agency (ASI, SIMBIO-SYS project) for the financial supports.

## References

Bandfield, J.L., Hamilton, V.E., Christensen, P.R., 2000. A Global View of Martian Surface Compositions from MGS-TES. Science (80-. ). 287, 1626–1630. https://doi.org/10.1126/science.287.5458.1626

Christensen, P.R., Bandfield, J.L., Hamilton, V.E., Howard, D.A., Lane, M.D., Piatek, J.L., Ruff, S.W., Stefanov, W.L., 2000. A thermal emission spectral library of rock-forming minerals. J. Geophys. Res. 105, 9735–9739. https://doi.org/10.1029/1998JE000624

Christensen, P.R., Bandfield, J.L., Hamilton, V.E., Ruff, S.W., Kieffer, H.H., Titus, T.N., Malin, M.C., Morris, R. V., Lane, M.D., Clark, R.L., Jakosky, B.M., Mellon, M.T., Pearl, J.C., Conrath, B.J., Smith, M.D., Clancy, R.T., Kuzmin, R.O., Roush, T., Mehall, G.L., Gorelick, N., Bender, K., Murray, K., Dason, S., Greene, E., Silverman, S., Greenfield, M., 2001. Mars Global Surveyor Thermal Emission Spectrometer experiment: Investigation description and surface science results. J. Geophys. Res. Planets 106, 23823–23871. https://doi.org/10.1029/2000JE001370

574 Christensen, P.R., Hamilton, V.E., Mehall, G.L., Pelham, D., O'Donnell, W., Anwar,
575 S., Bowles, H., Chase, S., Fahlgren, J., Farkas, Z., Fisher, T., James, O., Kubik,
576 I., Lazbin, I., Miner, M., Rassas, M., Schulze, L., Shamordola, K., Tourville, T.,
577 West, G., Woodward, R., Lauretta, D., 2018. The OSIRIS-REx Thermal
578 Emission Spectrometer (OTES) Instrument. Space Sci. Rev. 214, 87.
579 https://doi.org/10.1007/s11214-018-0513-6

580 Christensen, P.R., McSween, H.Y., Bandfield, J.L., Ruff, S.W., Rogers, A.D.,
581 Hamilton, V.E., Gorelick, N., Wyatt, M.B., Jakosky, B.M., Kieffer, H.H., Malin,
582 M.C., Moersch, J.E., 2005. Evidence for magmatic evolution and diversity on
583 Mars from infrared observations. Nature 436, 504–509.
584 https://doi.org/10.1038/nature03639

585 Conel, J.E., 1969. Infrared Emissivities of Silicates: Experimental Results and a
586 Cloudy Atmosphere Model of Spectral Emission from Condensed Particulate
587 Mediums. J. Geophys. Res. 74, 1614–1634.
588 https://doi.org/10.1029/JB074i006p01614

589 D'Amore, M., Helbert, J., Maturilli, A., Varatharajan, I., Ulmer, B., Säuberlich, T.,
590 Berlin, R., Peter, G., Hiesinger, H., Martinez, S., Casale, M., Ortiz de Landaluce,
591 I., Walter, I., 2018. Data processing of the Mercury radiometer and thermal
592 infrared imaging spectrometer (MERTIS) onboard Bepi Colombo, in: Strojnik,
593 M., Kirk, M.S. (Eds.), Infrared Remote Sensing and Instrumentation XXVI.
594 SPIE, p. 16. https://doi.org/10.1117/12.2321051

595 Donaldson Hanna, K.L., Cheek, L.C., Pieters, C.M., Mustard, J.F., Greenhagen, B.T.,
596 Thomas, I.R., Bowles, N.E., 2014. Global assessment of pure crystalline
597 plagioclase across the Moon and implications for the evolution of the primary

598 crust. J. Geophys. Res. Planets 119, 1516–1545.
599 https://doi.org/10.1002/2013JE004476

600 Donaldson Hanna, K.L., Thomas, I.R., Bowles, N.E., Greenhagen, B.T., Pieters,
601 C.M., Mustard, J.F., Jackson, C.R.M., Wyatt, M.B., 2012. Laboratory emissivity
602 measurements of the plagioclase solid solution series under varying
603 environmental conditions. J. Geophys. Res. E Planets 117, 1–7.
604 https://doi.org/10.1029/2012JE004184

605 E. Vander Kaaden, K., M. McCubbin, F., R. Nittler, L., N. Peplowski, P., Z. Weider,
606 S., A. Frank, E., J. McCoy, T., 2017. Geochemistry, mineralogy, and petrology
607 of boninitic and komatiitic rocks on the mercurian surface: Insights into the
608 mercurian mantle. Icarus 285, 155–168.
609 https://doi.org/10.1016/j.icarus.2016.11.041

610 Emery, J.P., Sprague, A.L., Witteborn, F.C., Colwell, J.E., Kozlowski, R.W.H.,
611 Wooden, D.H., 1998. Mercury: Thermal Modeling and Mid-infrared (5–12 μm)
612 Observations. Icarus 136, 104–123. https://doi.org/10.1006/ICAR.1998.6012

613 Farmer, V.C., 1974. The Infrared Spectra of Minerals. Mineralogical Society of Great
614 Britain and Ireland. https://doi.org/https://doi.org/10.1180/mono-4

615 Ferrari, S., Nestola, F., Massironi, M., Maturilli, A., Helbert, J., Alvaro, M.,
616 Domeneghetti, M.C., Zorzi, F., 2014. In-situ high-temperature emissivity spectra
617 and Thermal expansion of C2/c pyroxenes: Implications for the surface of
618 Mercury. Am. Mineral. 99, 786–792. https://doi.org/10.2138/am.2014.4698

619 Glotch, T.D., Lucey, P.G., Bandfield, J.L., Greenhagen, B.T., Thomas, I.R., Elphic,
620 R.C., Bowles, N., Wyatt, M.B., Allen, C.C., Hanna, K.D., Paige, D.A., 2010.
621 Highly silicic compositions on the moon. Science (80-. ). 329, 1510–1513.

https://doi.org/10.1126/science.1192148

Greenhagen, B.T., Lucey, P.G., Wyatt, M.B., Glotch, T.D., Allen, C.C., Arnold, J.A., Bandfield, J.L., Bowles, N.E., Hanna, K.L.D., Hayne, P.O., Song, E., Thomas, I.R., Paige, D.A., 2010. Global silicate mineralogy of the moon from the diviner lunar radiometer. Science (80-. ). 329, 1507–1509. https://doi.org/10.1126/science.1192196

Halliday, A.N., 2001. In the beginning. . . Nature 409, 144–145. https://doi.org/10.1038/35051685

Hamilton, V.E., 2010. Thermal infrared (vibrational) spectroscopy of Mg-Fe olivines: A review and applications to determining the composition of planetary surfaces. Chemie der Erde 70, 7–33. https://doi.org/10.1016/j.chemer.2009.12.005

Hamilton, V.E., 2000. Thermal infrared emission spectroscopy of the pyroxene mineral series. J. Geophys. Res. E Planets 105, 9701–9716. https://doi.org/10.1029/1999JE001112

Hamilton, V.E., Christensen, P.R., 2000. Determining the modal mineralogy of mafic and ultramafic igneous rocks using thermal emission spectroscopy. J. Geophys. Res. 105, 9717. https://doi.org/10.1029/1999JE001113

Helbert, J., Nestola, F., Ferrari, S., Maturilli, A., Massironi, M., Redhammer, G.J., Capria, M.T., Carli, C., Capaccioni, F., Bruno, M., 2013. Olivine thermal emissivity under extreme temperature ranges: Implication for Mercury surface. Earth Planet. Sci. Lett. 371–372, 252–257. https://doi.org/10.1016/j.epsl.2013.03.038

Hiesinger, H., Helbert, J., 2010. The Mercury Radiometer and Thermal Infrared Spectrometer (MERTIS) for the BepiColombo mission. Planet. Space Sci. 58,

144–165. https://doi.org/10.1016/J.PSS.2008.09.019

Lauretta, D.S., Balram-Knutson, S.S., Beshore, E., Boynton, W. V., Drouet d'Aubigny, C., DellaGiustina, D.N., Enos, H.L., Golish, D.R., Hergenrother, C.W., Howell, E.S., Bennett, C.A., Morton, E.T., Nolan, M.C., Rizk, B., Roper, H.L., Bartels, A.E., Bos, B.J., Dworkin, J.P., Highsmith, D.E., Lorenz, D.A., Lim, L.F., Mink, R., Moreau, M.C., Nuth, J.A., Reuter, D.C., Simon, A.A., Bierhaus, E.B., Bryan, B.H., Ballouz, R., Barnouin, O.S., Binzel, R.P., Bottke, W.F., Hamilton, V.E., Walsh, K.J., Chesley, S.R., Christensen, P.R., Clark, B.E., Connolly, H.C., Crombie, M.K., Daly, M.G., Emery, J.P., McCoy, T.J., McMahon, J.W., Scheeres, D.J., Messenger, S., Nakamura-Messenger, K., Righter, K., Sandford, S.A., 2017. OSIRIS-REx: Sample Return from Asteroid (101955) Bennu. Space Sci. Rev. 212, 925–984. https://doi.org/10.1007/s11214-017-0405-1

Lim, L.F., McConnochie, T.H., Bell, J.F., Hayward, T.L., 2005. Thermal infrared (8-13 μm) spectra of 29 asteroids: The Cornell Mid-Infrared Asteroid Spectroscopy (MIDAS) survey. Icarus 173, 385–408. https://doi.org/10.1016/j.icarus.2004.08.005

Lindh, A., Andersson, U.B., Lundqvist, T., Claesson, S., 2001. Evidence of crustal contamination of mafic rocks associated with rapakivi rocks: An example from the Nordingrå complex, Central Sweden. Geol. Mag. 138, 371–386. https://doi.org/10.1017/S0016756801005672

Logan, L.M., Hunt, G.R., Salisbury, J.W., Balsamo, S.R., 1973. Compositional implications of Christiansen frequency maximums for infrared remote sensing applications. J. Geophys. Res. 78, 4983–5003.

https://doi.org/10.1029/JB078i023p04983

Lyon, R.J.P., 1962. Evaluation of Infrared Spectrophotometry for Compositional Analysis of Lunar and Planetary Soils. Tech. report,Stanford Res. Inst.

Maturilli, A., Helbert, J., Moroz, L., 2008. The Berlin emissivity database (BED). Planet. Space Sci. 56, 420–425. https://doi.org/10.1016/j.pss.2007.11.015

Maturilli, A., Helbert, J., St. John, J.M., Head, J.W., Vaughan, W.M., D'Amore, M., Gottschalk, M., Ferrari, S., 2014. Komatiites as Mercury surface analogues: Spectral measurements at PEL. Earth Planet. Sci. Lett. 398, 58–65. https://doi.org/10.1016/j.epsl.2014.04.035

Maturilli, A., Helbert, J., Witzke, A., Moroz, L., 2006. Emissivity measurements of analogue materials for the interpretation of data from PFS on Mars Express and MERTIS on Bepi-Colombo. Planet. Space Sci. 54, 1057–1064. https://doi.org/10.1016/j.pss.2005.12.021

Mckay, D.S., Heiken, G., Basu, A., Blanford, G., Simon, S., Reedy, R., French, B.M., Papike, J., 1980. The lunar regolith, in: The Lunar Sourcebook. pp. 285–356.

Nakamura, T., Noguchi, T., Tanaka, M., Zolensky, M.E., Kimura, M., Tsuchiyama, A., Nakato, A., Ogami, T., Ishida, H., Uesugi, M., Yada, T., Shirai, K., Fujimura, A., Okazaki, R., Sandford, S.A., Ishibashi, Y., Abe, M., Okada, T., Ueno, M., Mukai, T., Yoshikawa, M., Kawaguchi, J., 2011. Itokawa dust particles: A direct link between S-type asteroids and ordinary chondrites. Science (80-. ). 333, 1113–1116. https://doi.org/10.1126/science.1207758

Namur, O., Charlier, B., 2017. Silicate mineralogy at the surface of Mercury. Nat. Geosci. 10, 9–13. https://doi.org/10.1038/ngeo2860

Paige, D.A., Siegler, M.A., Zhang, J.A., Hayne, P.O., Foote, E.J., Bennett, K.A.,

694 Vasavada, A.R., Greenhagen, B.T., Schofield, J.T., McCleese, D.J., Foote, M.C.,
695 DeJong, E., Bills, B.G., Hartford, W., Murray, B.C., Allen, C.C., Snook, K.,
696 Soderblom, L.A., Calcutt, S., Taylor, F.W., Bowles, N.E., Bandfield, J.L.,
697 Elphic, R., Ghent, R., Glotch, T.D., Wyatt, M.B., Lucey, P.G., 2010. Diviner
698 Lunar Radiometer Observations of Cold Traps in the Moon's South Polar
699 Region. Science (80-. ). 330, 479 LP-482.

700 Pouchou, J.-L., Pichoir, F., 1991. Quantitative Analysis of Homogeneous or Stratified
701 Microvolumes Applying the Model "PAP," in: Electron Probe Quantitation.
702 Springer US, Boston, MA, pp. 31–75. https://doi.org/10.1007/978-1-4899-2617-
703 3_4

704 Ramsey, M.S., Christensen, P.R., 1998. Mineral abundance determination:
705 Quantitative deconvolution of thermal emission spectra. J. Geophys. Res. Solid
706 Earth 103, 577–596. https://doi.org/10.1088/1475-7516/2016/07/026

707 Rietveld, H.M., 1967. Line profiles of neutron powder-diffraction peaks for structure
708 refinement. Acta Crystallogr. 22, 151–152.
709 https://doi.org/10.1107/S0365110X67000234

710 Salisbury, J.W., D'Aria, D.M., 1994. Emissivity of terrestrial materials in the 3-5 μm
711 atmospheric window. Remote Sens. Environ. 47, 345–361.
712 https://doi.org/doi.org/10.1016/0034-4257(94)90102-3

713 Salisbury, J.W., Wald, A., 1992. The role of volume scattering in reducing spectral
714 contrast of reststrahlen bands in spectra of powdered minerals. Icarus 96, 121–
715 128. https://doi.org/10.1016/0019-1035(92)90009-V

716 Salisbury, J.W., Walter, L.S., 1989. Thermal infrared (2.5-13.5 μm) spectroscopic
717 remote sensing of igneous rock types on particulate planetary surfaces. J.

718 Geophys. Res. 94, 9192–9202. https://doi.org/10.1029/JB094iB07p09192

719 Smith, J. V., Brown, W.L., 1988. Feldspar Minerals : Volume 1 Crystal Structures,
720 Physical, Chemical, and Microtextural Properties. Springer Berlin Heidelberg.

721 Sprague, A.L., Donaldson Hanna, K.L., Kozlowski, R.W.H., Helbert, J., Maturilli, A.,
722 Warell, J.B., Hora, J.L., 2009. Spectral emissivity measurements of Mercury's
723 surface indicate Mg- and Ca-rich mineralogy, K-spar, Na-rich plagioclase, rutile,
724 with possible perovskite, and garnet. Planet. Space Sci. 57, 364–383.
725 https://doi.org/10.1016/j.pss.2009.01.006

726 Tonks, W.B., Melosh, H.J., 1993. Magma ocean formation due to giant impacts. J.
727 Geophys. Res. Planets 98, 5319–5333. https://doi.org/10.1029/92JE02726

728 Tribaudino, M., Angel, R.J., Cámara, F., Nestola, F., Pasqual, D., Margiolaki, I.,
729 2010. Thermal expansion of plagioclase feldspars. Contrib. to Mineral. Petrol.
730 160, 899–908. https://doi.org/10.1007/s00410-010-0513-3

731 Vernazza, P., Carry, B., Emery, J., Hora, J.L., Cruikshank, D., Binzel, R.P., Jackson,
732 J., Helbert, J., Maturilli, A., 2010. Mid-infrared spectral variability for
733 compositionally similar asteroids: Implications for asteroid particle size
734 distributions. Icarus 207, 800–809. https://doi.org/10.1016/j.icarus.2010.01.011

735 Wald, A.E., Salisbury, J.W., 1995. Thermal infrared directional emissivity of
736 powdered quartz. J. Geophys. Res. Solid Earth 100, 24665–24675.
737 https://doi.org/10.1029/95JB02400

738 Wetherill, G.W., 1980. Formation of the Terrestrial Planets. Annu. Rev. Astron.
739 Astrophys. 18, 77–113. https://doi.org/10.1146/annurev.aa.18.090180.000453

740

741 **Table 1 Suppl. Mat.** Results of the X-ray powder diffraction analysis of the Nordingrå-complex

742 anothosite sample.

| Mineral | wt. % |
|---|---|
| **Andesine, labradorite** | 83 |
| **Quartz** | 6 |
| **Diopside - ferroan** | 6 |
| **Actinolite** | 3 |
| **Ilmenite** | <1 |
| **Clinochlore** | <1 |

743

744

745 **Table 2 Suppl. Mat.** Electron microprobe analysis (oxide wt. %) and formula in atoms per
746 formula unit based on six oxygen atoms for the crystals studied in this work. Standards (analytical
747 crystals, spectral lines) used were albite (Amelia plagioclase, TAP, Kα) for Na, MgO (TAP, Kα)
748 for Mg, $Al_2O_3$ (TAP, Kα) for Al, diopside (TAP, Kα) for Si and (PET, Kα) for Ca, $MnTiO_3$ (PET,
749 Kα) for Ti and (LIF 220, Kα) for Mn, $Cr_2O_3$ (LIF 220, Kα) for Cr, $Fe_2O_3$ (LIF 220, Kα) for Fe, and
750 orthoclase (PET, Kα) for K.

| Sample | Plagioclase | Plagioclase (core) | Clinopyroxene Mg#0.52 | Clinopyroxene Mg#0.33 |
|---|---|---|---|---|
| **Oxide wt.%** | | | | |
| **$Na_2O$** | 6.05 | 4.29 | 0.21 | 0.13 |
| **MgO** | 0.02 | 0.02 | 10.00 | 6.49 |
| **$Al_2O_3$** | 26.56 | 29.28 | 1.75 | 0.77 |
| **$SiO_2$** | 56.84 | 52.67 | 50.50 | 49.99 |
| **$K_2O$** | 0.57 | 0.43 | - | - |
| **CaO** | 9.07 | 12.34 | 20.65 | 20.57 |
| **$TiO_2$** | 0.04 | 0.06 | 0.64 | 0.33 |
| **$Cr_2O_3$** | 0.01 | 0.01 | 0.03 | 0.01 |
| **MnO** | 0.01 | 0.01 | 0.38 | 0.44 |
| **FeO** | - | - | 16.44 | 21.97 |
| **$Fe_2O_3$** | 0.30 | 0.33 | - | - |
| **Total** | 99.45 | 99.44 | 100.60 | 100.70 |
| **Formula** | | | | |
| **Ca** | 0.44 | 0.60 | 0.85 | 0.87 |
| **Na** | 0.53 | 0.38 | 0.02 | 0.01 |
| **K** | 0.03 | 0.02 | - | - |
| **Mn** | - | - | 0.01 | 0.01 |
| **$Fe^{2+}$** | - | - | 0.53 | 0.72 |
| **$Fe^{3+}$** | 0.01 | 0.01 | - | - |
| **Mg** | - | - | 0.56 | 0.38 |
| **Ti** | - | - | 0.02 | 0.01 |
| **Cr** | - | - | - | - |
| **Al** | 1.42 | 1.58 | 0.08 | 0.04 |
| **Si** | 2.57 | 2.40 | 1.94 | 1.97 |
| **Total** | 4.00 | 4.00 | 4.00 | 4.01 |

751

752

753 **Table 1.** Samples obtained by bulk sample separation and mixing of the two main phases,
754 plagioclases and clinopyroxene.

| | | Plagioclase | Clinopyroxene |
|---|---|---|---|
| **Sample** | **Label** | **wt. %** | **wt. %** |
| **Anorthosite** | *anorth* | 83 ($93_{pl\text{-}cpx}$) | 6 ($7_{pl\text{-}cpx}$) |
| **Plagioclase** | *pl100* | 100 | - |
| **Synthetic anorthosite** | *pl090* | 90 | 10 |
| **Synthetic gabbros** | *pl050* | 50 | 50 |
| **Clinopyroxene** | *pl000* | - | 100 |

755

756

757 **Table 2.** Positions of Christiansen features, Reststrahlen bands and Transparency features of reflectance-derived emissivity spectra collected at

758 295 K.

| | | Feature position | | | | | | | | | | | |
|---|---|---|---|---|---|---|---|---|---|---|---|---|---|
| | | $cm^{-1}$ | | | | | | | | | | | |
| **Sample** | **Label** | **CF** | **CF** | **RB** | **RB** | **RB** | **RB** | **RB** | **RB** | **RB** | **RB** | **TF** | **TF** |
| **Anorthosite** | *anorth* | 1265 | - | 1188 | 1120 | - | - | 1001 | - | - | - | 874 | - |
| **Plagioclase** | *pl100* | 1263 | - | 1180 | 1136 | - | - | 1003 | - | 920 | - | 874 | - |
| **Synthetic anorthosite** | *pl090* | 1259 | - | 1178 | 1132 | - | - | 1001 | (941) | 923 | - | 877 | - |
| **Synthetic gabbros** | *pl050* | 1246 | - | 1173 | - | 1101 | - | - | 958 | 912 | - | 879 | - |
| **Clinopyroxene** | *pl000* | - | 1159 | - | - | - | 1097 | - | 960 | - | 866 | - | 831 |
| | | | | *a* | | *b* | | *c* | | | *d* | | |

759

760

761 **Table 3.** Emissivity of Christiansen features, Reststrahlen bands and Transparency features of reflectance-derived emissivity spectra collected at

| | | Emissivity | | | | | | | | | | | |
|---|---|---|---|---|---|---|---|---|---|---|---|---|---|
| **Sample** | **Label** | **CF** | **CF** | **RB** | **RB** | **RB** | **RB** | **RB** | **RB** | **RB** | **RB** | **TF** | **TF** |
| **Anorthosite** | *anorth* | 0.983 | - | 0.955 | 0.954 | - | - | 0.956 | - | - | - | 0.951 | - |
| **Plagioclase** | *pl100* | 0.996 | - | 0.963 | 0.962 | - | - | 0.958 | - | 0.958 | - | 0.952 | - |
| **Synthetic anorthosite** | *pl090* | 0.993 | - | 0.957 | 0.956 | - | - | 0.955 | (0.954) | 0.954 | - | 0.954 | - |
| **Synthetic gabbros** | *pl050* | 0.983 | - | 0.964 | - | 0.950 | - | - | 0.939 | 0.939 | - | 0.938 | - |
| **Clinopyroxene** | *pl000* | - | 0.984 | - | - | - | 0.958 | - | 0.964 | - | 0.961 | - | 0.960 |
| | | | | *a* | | *b* | | *c* | | | *d* | | |

762 295 K.

763

764

765 **Table 4.** Positions of Christiansen features, Reststrahlen bands and Transparency features of emissivity spectra collected at different
766 temperatures.

| | | Temp. | Feature position | | | | | | | | | | |
|---|---|---|---|---|---|---|---|---|---|---|---|---|---|
| | | K | $cm^{-1}$ | | | | | | | | | | |
| **Sample** | **Label** | | **CF** | **CF** | **RB** | **RB** | **RB** | **RB** | **RB** | **RB** | **RB** | **RB** | **TF** | **TF** |
| **Anorthosite** | *anorth* | **425** | 1280 | - | 1188 | 1140 | - | - | 992 | - | 915 | - | 875 | - |
| | | **525** | 1295 | - | 1175 | 1139 | - | - | 989 | - | 914 | - | 874 | - |
| | | **625** | 1296 | - | 1172 | 1136 | - | - | 989 | - | 914 | - | 878 | - |
| | | **725** | 1305 | - | 1165 | 1133 | - | - | 987 | - | 918 | - | - | - |
| **Plagioclase** | *pl100* | **425** | 1291 | - | 1179 | 1146 | - | - | 986 | - | 912 | - | 874 | - |
| | | **525** | 1294 | - | 1173 | 1146 | - | - | 989 | - | 914 | - | 872 | - |
| | | **625** | 1303 | - | - | 1140 | - | - | 989 | - | 913 | - | 875 | - |
| | | **725** | 1314 | - | - | 1136 | - | - | 985 | - | 915 | - | - | - |
| **Synthetic anorth.** | *pl090* | **425** | 1287 | - | 1185 | 1148 | - | - | 985 | - | 913 | - | 876 | - |
| | | **525** | 1287 | - | 1172 | 1142 | - | - | 988 | - | 914 | - | 874 | - |
| | | **625** | 1294 | - | 1166 | 1139 | - | - | 988 | - | 914 | - | 875 | - |
| | | **725** | 1300 | - | - | 1132 | - | - | 988 | - | 914 | - | - | - |
| **Synthetic gabbro** | *pl050* | **425** | 1240 | - | 1188 | - | 1111 | - | 976 | - | 906 | 875 | - | 823 |
| | | **525** | 1248 | - | 1180 | - | 1108 | - | 985 | - | 908 | 860 | - | 823 |
| | | **625** | 1262 | - | 1170 | - | 1104 | - | 985 | - | 908 | 859 | - | 820 |
| | | **725** | 1273 | - | 1163 | - | 1096 | - | 984 | - | 908 | 859 | - | 819 |
| **Clinopyroxene** | *pl000* | **425** | - | 1160 | - | - | - | 1106 | - | 959 | | 872 | - | 811 |
| | | **525** | - | 1162 | - | - | - | 1103 | - | 954 | | 863 | - | 811 |
| | | **625** | - | 1163 | - | - | - | 1095 | - | 950 | | 860 | - | 807 |
| | | **725** | - | 1187 | - | - | - | 1086 | - | 947 | | 857 | - | 805 |

| | | | | | *a* | | *b* | | *c* | | | *d* | | |
|---|---|---|---|---|---|---|---|---|---|---|---|---|---|---|

767 **Table 5.** Emissivity of Christiansen features, Reststrahlen bands and Transparency features of spectra collected at different temperatures.

| | | **Temp.** | **Emissivity** | | | | | | | | | | | |
|---|---|---|---|---|---|---|---|---|---|---|---|---|---|---|
| | | **K** | | | | | | | | | | | | |
| **Sample** | **Label** | | **CF** | **CF** | **RB** | **RB** | **RB** | **RB** | **RB** | **RB** | **RB** | **RB** | **TF** | **TF** |
| **Anorthosite** | *anorth* | **425** | 0.987 | - | 0.968 | 0.971 | - | - | 0.976 | - | 0.975 | - | 0.973 | - |
| | | **525** | 0.985 | - | 0.957 | 0.958 | - | - | 0.963 | - | 0.964 | - | 0.963 | - |
| | | **625** | 0.988 | - | 0.953 | 0.952 | - | - | 0.956 | - | 0.957 | - | 0.957 | - |
| | | **725** | 0.982 | - | 0.943 | 0.940 | - | - | 0.944 | - | 0.946 | - | - | - |
| **Plagioclase** | *pl100* | **425** | 0.995 | - | 0.967 | 0.969 | - | - | 0.971 | - | 0.967 | - | 0.964 | - |
| | | **525** | 0.994 | - | 0.958 | 0.959 | - | - | 0.960 | - | 0.958 | - | 0.955 | - |
| | | **625** | 0.996 | - | - | 0.949 | - | - | 0.949 | - | 0.947 | - | 0.947 | - |
| | | **725** | 0.992 | - | - | 0.936 | - | - | 0.934 | - | 0.932 | - | - | - |
| **Synthetic anorth.** | *pl090* | **425** | 0.992 | - | 0.968 | 0.969 | - | - | 0.971 | - | 0.968 | - | 0.966 | - |
| | | **525** | 0.989 | - | 0.957 | 0.957 | - | - | 0.958 | - | 0.956 | - | 0.954 | - |
| | | **625** | 0.987 | - | 0.947 | 0.946 | - | - | 0.947 | - | 0.945 | - | 0.945 | - |
| | | **725** | 0.992 | - | - | 0.942 | - | - | 0.939 | - | 0.936 | - | - | - |
| **Synthetic gabbro** | *pl050* | **425** | 0.984 | - | 0.976 | - | 0.978 | - | 0.979 | - | 0.976 | 0.974 | - | 0.974 |
| | | **525** | 0.980 | - | 0.969 | - | 0.969 | - | 0.972 | - | 0.969 | 0.968 | - | 0.967 |
| | | **625** | 0.984 | - | 0.968 | - | 0.966 | - | 0.968 | - | 0.965 | 0.964 | - | 0.964 |
| | | **725** | 0.981 | - | 0.962 | - | 0.958 | - | 0.961 | - | 0.958 | 0.958 | - | 0.958 |
| **Clinopyroxene** | *pl000* | **425** | - | 0.989 | - | - | - | 0.976 | - | 0.980 | | 0.974 | - | 0.972 |
| | | **525** | - | 0.984 | - | - | - | 0.968 | - | 0.974 | | 0.969 | - | 0.966 |
| | | **625** | - | 0.985 | - | - | - | 0.967 | - | 0.971 | | 0.965 | - | 0.963 |
| | | **725** | - | 0.983 | - | - | - | 0.961 | - | 0.965 | | 0.959 | - | 0.957 |

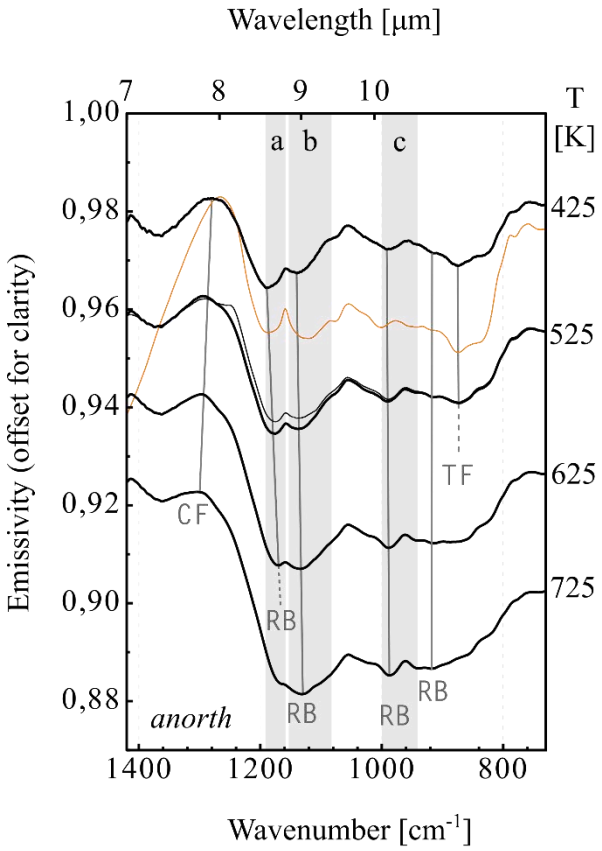


**Figure 1.** Anorthosite *talquale* emissivity spectra ($\varepsilon_a$, black lines) collected at 4 temperatures are shown alongside derived emissivity ($\varepsilon_d$, orange lines) collected at 295 K; emissivity spectra were collected with increasing temperatures (black thick lines), then during the cooling maintaining the temperature at 525 K (black thin line). Wavelength ranges where RBs occur are indicated by coloured windows.

773 **Figure 2.** Endmembers and mixtures emissivity spectra ($\varepsilon_a$, black lines) collected at 4 temperatures are shown alongside derived emissivity ($\varepsilon_d$,
774 orange lines) collected at 295 K; emissivity spectra were collected with increasing temperatures (black thick lines), then during the cooling
775 maintaining the temperature at 525 K (black thin line). Results are shown, from left to right, with decreasing degree of polymerization.
776 Wavelength ranges where RBs occur are indicated by grey windows and labelled a, b, c and d.

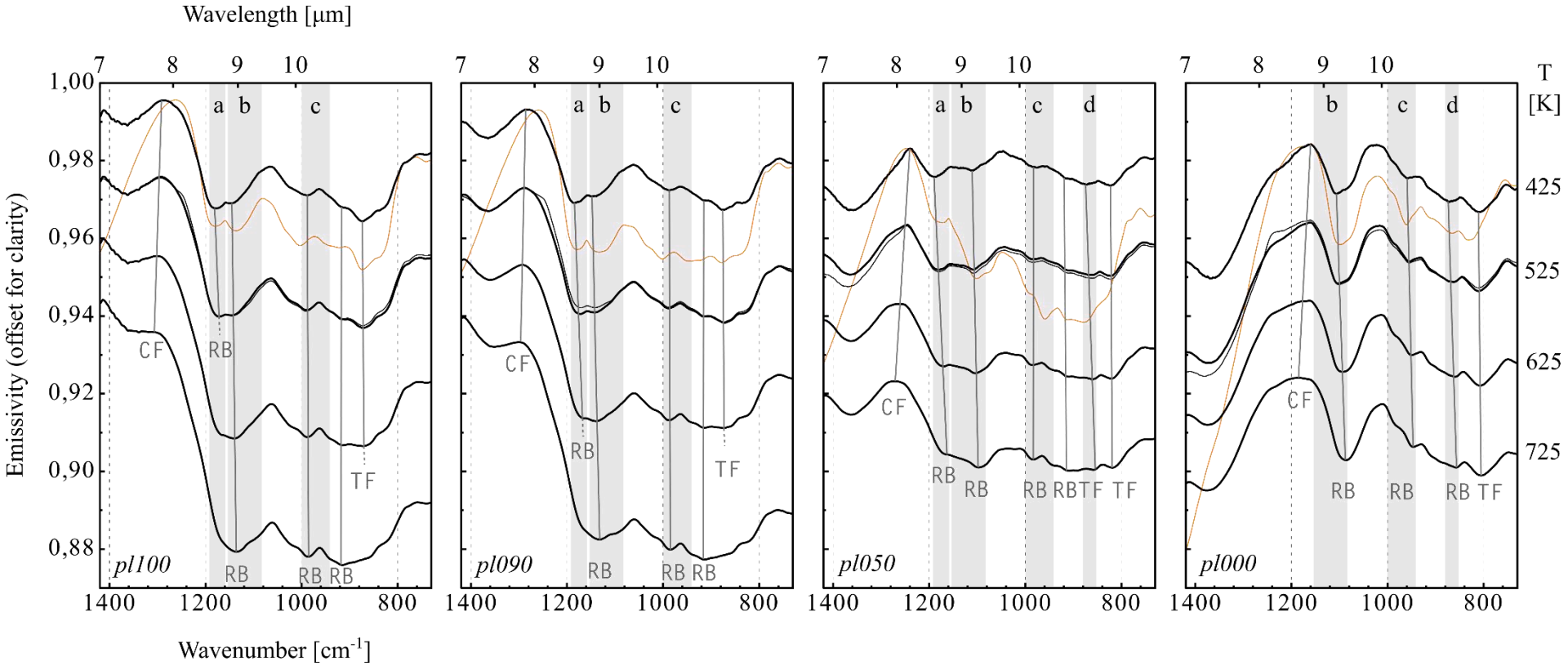


777

778

779 **Figure 3.** Comparison between emissivity CF positions collected at 425 K, 525 K, 625 K and 725 K (upper panel) and in function of the

780 plagioclase content (lower panel).

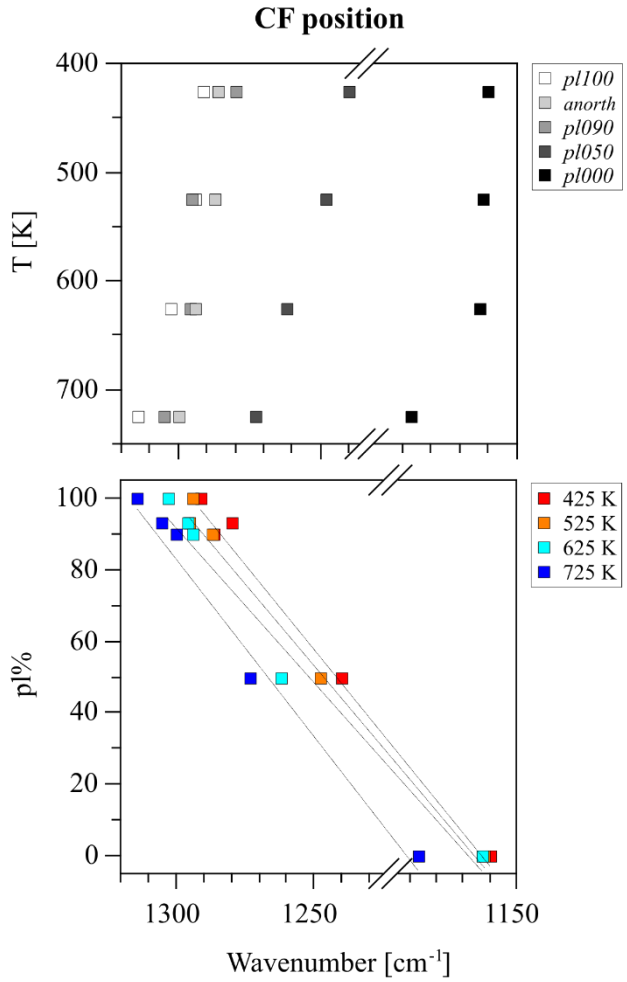


781

**Figure 4.** RBs positions in function of the temperature (upper panels a-c) and the plagioclase content (lower panels d-f): RBs are grouped in function of the wavelength range where they occur.

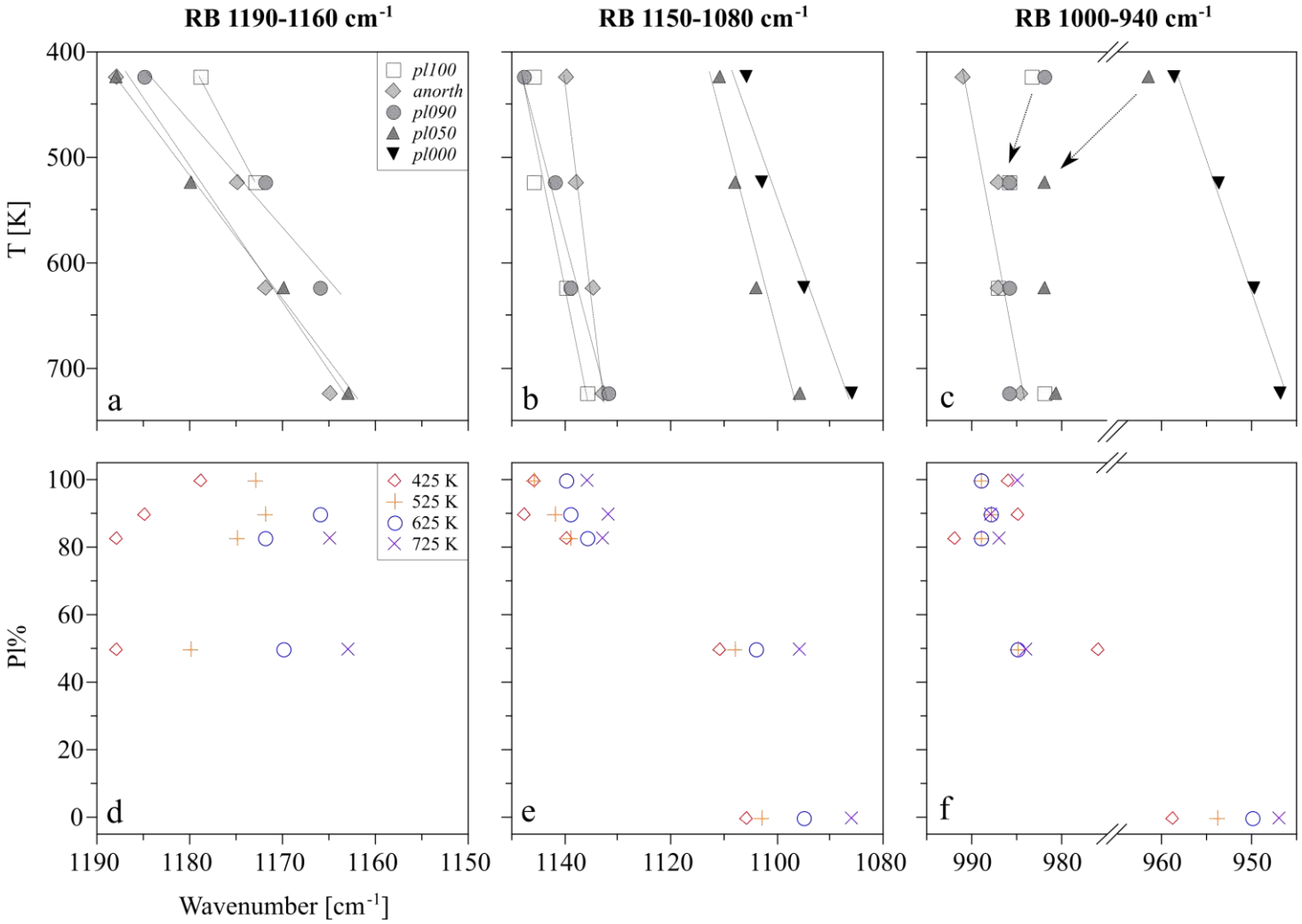

**Figure 5.** RBs depths in function of the temperature (upper panels a-c) and of the plagioclase content (lower panels d-f): RBs are grouped in function of the wavelength range where they occur.